Modern Electronic Materials 2023; 9(2): 57–68
DOI 10.3897/j.moem.9.2.109980

Research Article

Electron and hole injection barriers between silicon substrate and RF magnetron sputtered In_2O_3 : Er films

Konstantin V. Feklistov[1,6], Aleksey G. Lemzyakov[2], Alexander A. Shklyaev[1,4], Dmitry Yu. Protasov[1,5], Alexander S. Deryabin[1], Evgeny V. Spesivsev[1], Dmitry V. Gulyaev[1], Alexey M. Pugachev[3], Dmitriy G. Esaev[1]

1 *Rzhanov Institute of Semiconductor Physics, Siberian Branch of the Russian Academy of Sciences, 13 Acad. Lavrentieva Ave., Novosibirsk 630090, Russian Federation*
2 *Budker Institute of Nuclear Physics, Siberian Branch of the Russian Academy of Sciences, 11 Acad. Lavrentieva Ave., Novosibirsk 630090, Russian Federation*
3 *Institute of Automation and Electrometry, Siberian Branch of the Russian Academy of Sciences, 1 Acad. Koptyug Ave., Novosibirsk 630090, Russian Federation*
4 *Novosibirsk State University, 1 Pirogova Str., Novosibirsk 630090, Russian Federation*
5 *Novosibirsk State Technical University, 20 Karla Marksa Ave., Novosibirsk 630073, Russian Federation*
6 *Academ Infrared LLC, 9 Uchenykh Str., Novosibirsk 630090, Russian Federation*

Corresponding author: Konstantin V. Feklistov (kos@isp.nsc.ru)

Received 30 May 2023 ♦ **Accepted** 22 June 2023 ♦ **Published** 5 July 2023

Citation: Feklistov KV, Lemzyakov AG, Shklyaev AA, Protasov DYu, Deryabin AS, Spesivsev EV, Gulyaev DV, Pugachev AM, Esaev DG (2023) Electron and hole injection barriers between silicon substrate and RF magnetron sputtered In_2O_3 : Er films. *Modern Electronic Materials* 9(2): 57–68. https://doi.org/10.3897/j.moem.9.2.109980

Abstract

In_2O_3 : Er films have been synthesized on silicon substrates by RF magnetron sputter deposition. The currents through the synthesized metal/oxide/semiconductor (MOS) structures (Si/In_2O_3 : Er/In-contact) have been measured for *n* and *p* type conductivity silicon substrates and described within the model of majority carrier thermoemission through the barrier, with bias voltage correction to the silicon potential drop. The electron and hole injection barriers between the silicon substrate and the film have been found to be 0.14 and 0.3 eV, respectively, by measuring the temperature dependence of the forward current at a low sub-barrier bias. The resulting low hole injection barrier is accounted for by the presence of defect state density spreading from the valence band edge into the In_2O_3 : Er band gap to form a hole conduction channel. The presence of defect state density in the In_2O_3 : Er band gap is confirmed by photoluminescence data in the respective energy range 1.55–3.0 eV. The band structure of the Si/In_2O_3 : Er heterojunction has been analyzed. The energy gap between the In_2O_3 : Er conduction band electrons and the band gap conduction channel holes has been estimated to be 1.56 eV.

Keywords

silicon, indium oxide, erbium, thin films, heterojunction, band structure, band discontinuity, barrier, injection, thermoemission, electrons, holes

1. Introduction

The integration of fiber-optic data communication systems directly in processors will seemingly be the next development step of computing systems. In 2015 a CPU was demonstrated featuring core-memory data exchange via a single fiber-optic line by means of an external laser [1, 2]. Industrial implementation of this system requires integration of light-emitting diodes **(LED)** with a wavelength within the transparency window of fiber-optic lines (1.5 μm) inside the CPU, i.e., on silicon [3, 4].

The common approach to this task world over is to employ a complex technological process of transferring a proven A3-B5 LED material (InGaAs) to a silicon substrate, by either transferring and bonding to the substrate [3, 4], or direct growth on the substrate by molecular beam epitaxy **(MBE)** [3, 5, 6]. This process is complex and expensive but reliable and promising. Currently research in this domain is focused on avoiding degradation, i.e., aging of the material [6–8]. A prominent result was achieved: a LED remaining stable over continuous operation at 80 °C for 1200 h, from which the LED time to failure was extrapolated to be 22 years [9]. Despite the encouraging success in this endeavor, the above cited time to failure estimate still has to be confirmed, especially for up to 90 °C CPU operation conditions. However the complexity and high cost of A3-B5 technology transfer to silicon still delays the industrial application of this process in CPUs and gives impetus for the research community to explore alternative solutions that may be less efficient than $A^{III}B^{V}$ technologies but cheaper.

One technologically simple and cheap alternative is the use of erbium ions Er^{3+} having the 1.54 μm wavelength $^4I_{13/2} \rightarrow {}^4I_{15/2}$ intracenter transition [10, 11] in the transparency window of fiber-optic lines.

Starting from the earliest works by H. Ennen [12], a direct approach has been developed, i.e., direct erbium atom incorporation in silicon (Si : Er) [13–16]. This approach has the advantage of simplicity and compatibility with silicon technologies. However, despite the appreciable effort of the international research community, LEDs synthesized employing this approach had too low quantum efficiency [15, 16] for practical implementation. One origin of this drawback was the technological complexity of heavy silicon doping with erbium atoms in an optically active state [13, 17, 18]. Another unresolved issue is thermal quenching of photoluminescence **(PL)** at room temperature as a result of reverse de-excitation of erbium ions generating electron-hole pairs in silicon lattice without photon emission (the so-called back transfer) [13, 19, 20].

It is well-known from literature that erbium de-excitation processes observed in silicon are suppressed in dielectrics since erbium PL occurs at room temperature in a wide range of dielectrics [13]. This is the fundamental operation principle of fiber-optic lasers and amplifiers with Er atoms in SiO_2 based dielectric optic fiber [21]. The difference is that Er is excited in the optic fiber by external A3-B5 LEDs. However, Er should be electrically excited by passing current. Electroluminescence **(EL)** was demonstrated earlier for erbium and a range of other rare-earth elements in silicon oxide [22, 23] and other dielectrics such as Si_3N_4 [24], TiO_2 [25] etc. upon hot-electron impact excitation in strong electric fields. The high-energy electron impact excitation cross-section for erbium was found to be $6 \cdot 10^{-15}$ cm^{-2} [22]. However, the high electron injection barrier between silicon and these dielectrics (~3.2 eV for Si/SiO_2) leads to low injection currents and high working electric fields [22–24]. Furthermore, hot electron impact excitation of erbium has a very low efficiency as compared with electron-hole pair recombination excitation.

There were a number of works demonstrating the possibility of generating room temperature EL of Er ions in optically transparent oxides, e.g. ZnO [26] and TiO_2 [27], where Er is excited by the electron-hole pair recombination mechanism. However, the lattice defect ZnO band gap levels proved to be optically active in the visible range [26]. In TiO_2, the lattice defect band gap levels excite the visible range Er^{3+} levels [27]. This makes the fundamental infrared **(IR)** 1.54 μm emission in these oxides inefficient. The above-cited works state the problem of choosing a more suitable oxide for erbium atom excitation by the efficient electron-hole pair recombination mechanism. The test oxide was erbium doped indium oxide ($In_2O_3 : Er$). This choice was based on the fact that room-temperature PL of Er in indium oxide was observed earlier [28, 29], e.g. by us [30]. Its related material ITO ($In_2O_3 : SnO_2$) is well-known and was tested in the synthesis of optically transparent conducting layers [31, 32].

The first problem to be solved is to develop conditions for the injection of both carrier types (electrons and holes) from silicon to $In_2O_3 : Er$ films. This requires finding the height of the carrier injection barriers at the $Si/In_2O_3 : Er$ heterointerface. Literary data on band discontinuity at the Si/In_2O_3 heterointerface are scarce and very inconsistent. Theoretical calculation yielded a negative electron injection barrier between silicon and indium oxide [33]. Open circuit voltage and short circuit current measurements for a Si/In_2O_3 heterointerface solar cell showed the electron affinity of In_2O_3 to be 4.45 eV [34]. Comparison with the electron affinity of Si (4.05 eV) also yields a negative electron injection barrier. However, the same work [33] contains a reference to unpublished Si/In_2O_3 electron injection barrier data of +0.61 eV. For the related material on the p-$Si/In_2O_3 : Mo$ heterostructure, I–V measurements showed the conduction band discontinuity to be +0.86 eV [35]. Despite the noticeable scatter of literary data, one can expect the electron injection barrier to Si/In_2O_3 to be low, taking into account the intrinsic n type of conductivity of undoped In_2O_3 [36, 37] originating from its intrinsic defects, i.e., oxygen vacancies, as well as the well-known application of n type conductivity doped $In_2O_3 : SnO_2$ (ITO) in optically transparent conducting layers and contacts [31, 32].

In the previous work [30] the Authors found the electron injection barrier between n type conductivity silicon substrates and $In_2O_3:Er$ films to be $\Phi_{ef} = 0.14$ eV (Fig. 1). This barrier is low and electrons can easily be injected through it. However, the magnitude of this barrier questions the possibility of hole injection from silicon. Proceeding from the well-known literary data on the silicon band gap $E_{gSi} = 1.12$ eV and the indium oxide fundamental band gap $E_{gIn_2O_3} = 2.69 \div 2.93$ eV [38, 39], the hole injection barrier between silicon and $In_2O_3:Er$ film should be equal to the valence band (E_V) discontinuity between these materials, i.e., approximately 1.64 eV (see Fig. 1 *b*). That high hole injection barrier makes it seemingly impossible at a first glance to achieve simultaneous opposite injection and transport of electrons and holes in $In_2O_3:Er$ films.

The aim of this work is to find, using direct electrical methods, the hole injection barrier between the p type conductivity silicon substrate and the films (Φ_{hf} for p-Si/$In_2O_3:Er$) and correct the band structure of the Si/$In_2O_3:Er$ heterointerface taking into account the estimated electron and hole injection barriers.

2. Experimental

$In_2O_3:$ Er were sputtered onto n and p type conductivity (100) silicon substrates (KEF 7.5 and KDB 7.5, respectively). For back contact doping the back sides of the n and p type conductivity substrates were implanted with 10^{15} cm^{-2} 100 keV As$^+$ ions and 10^{15} cm^{-2} 30 keV B$^+$ ions, respectively, and heat-treated at 1000 °C for 1 h in an inert argon (Ar) gas atmosphere. Before film deposition the silicon substrates were RCA chemically treated [40].

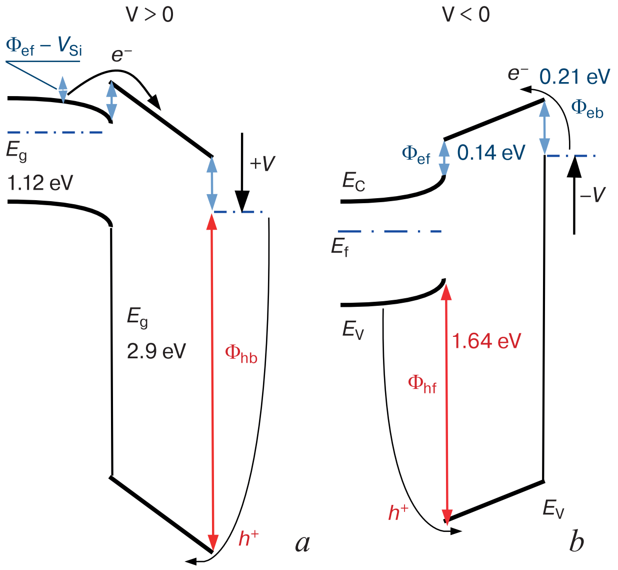

Figure 1. Schematic band diagrams of n-Si/$In_2O_3:Er$ heterostructure for (*a*) forward and (*b*) reverse bias showing earlier estimated [30] electron injection barrier 1 between silicon and $In_2O_3:Er$ film (0.14 eV) and barrier 2 between surface indium contact and film (0.21 eV)

$In_2O_3:Er$ films were deposited onto silicon substrates by RF magnetron sputter deposition on a BOC Edwards Auto 500 plant from an $In_2O_3:Er$ target containing 1% erbium. The main deposition mode was as follows:

- Ar flow 8 sccm, O_2 flow 2 sccm (1 sccm = standard cm^3/min);
- chamber working pressure $P = 6 \cdot 10^{-3}$ mbar;
- magnetron power $W_{RF} = 120$ W;
- power unit frequency 13.56 MHz;
- substrate temperature 100 °C;
- deposition time $t = 50$ min.

This deposition mode produced 200 nm $In_2O_3:Er$ films on n type conductivity substrates. 60 nm $In_2O_3:Er$ films were deposited on p type conductivity substrates under different conditions, i.e., Ar flow 20 sccm, O_2 flow 20 sccm, $W_{RF} = 100$ W, but the final film structure proved to be the same.

The microstructure of the films [30] represents an array of ~10 nm diam. nanowires densely grouped in bunches (discrete 50–100 nm diam. nanorods) spreading from the substrate to the film surface. All the nanowires have a body-centered cubic (bcc) In_2O_3 lattice (PDF No. 01-071-2194) but each nanowire has an individual orientation [30].

Top metallic indium contacts were applied through a 0.7 × 0.7 mm^2 mask. The back-side contacts were produced by In sputtering without masks on the whole back surface area.

The I–V curves and their temperature functions for the Si/$In_2O_3:Er$/In-contact structures were recorded on Keithley 4200-SCS and Keithley 2400 equipment fitted with Linkam LTS420E PB4 temperature control modules.

Steady-state PL was excited with a 325 nm He–Cd laser, power density 1 W/cm^2. The emission spectrum was recorded with an SDL-1 double monochromator spectrometer fitted with a photomultiplier at room temperature.

3. Results and discussion

3.1. I–V curves of n-Si/$In_2O_3:Er$ structure

Figure 2 *a* shows the I–V curve of structures on n type conductivity silicon substrates (n-Si/$In_2O_3:Er$) for room temperature and 300, 350 and 360 K. At a low positive (forward) top contact bias (0 to +0.5 V) the current through the structure is controlled by electron injection from n type conductivity silicon over a forward barrier (Φ_{ef}) at the Si/$In_2O_3:Er$ interface to the film (the so-called sub-barrier mode, Fig. 1 *a*). Since the barrier height decreases due to the applied bias ($\Phi_{ef} - V_{Si}$, where V_{Si} is the silicon potential drop, Fig. 1 *a*), the current through the barrier exhibits an exponential growth depending on the bias. Furthermore, the sub-barrier current through the barrier increases with temperature (Fig. 2 *a*) in the $0 < V < 0.5$ rang. This growth is controlled by the high-en-

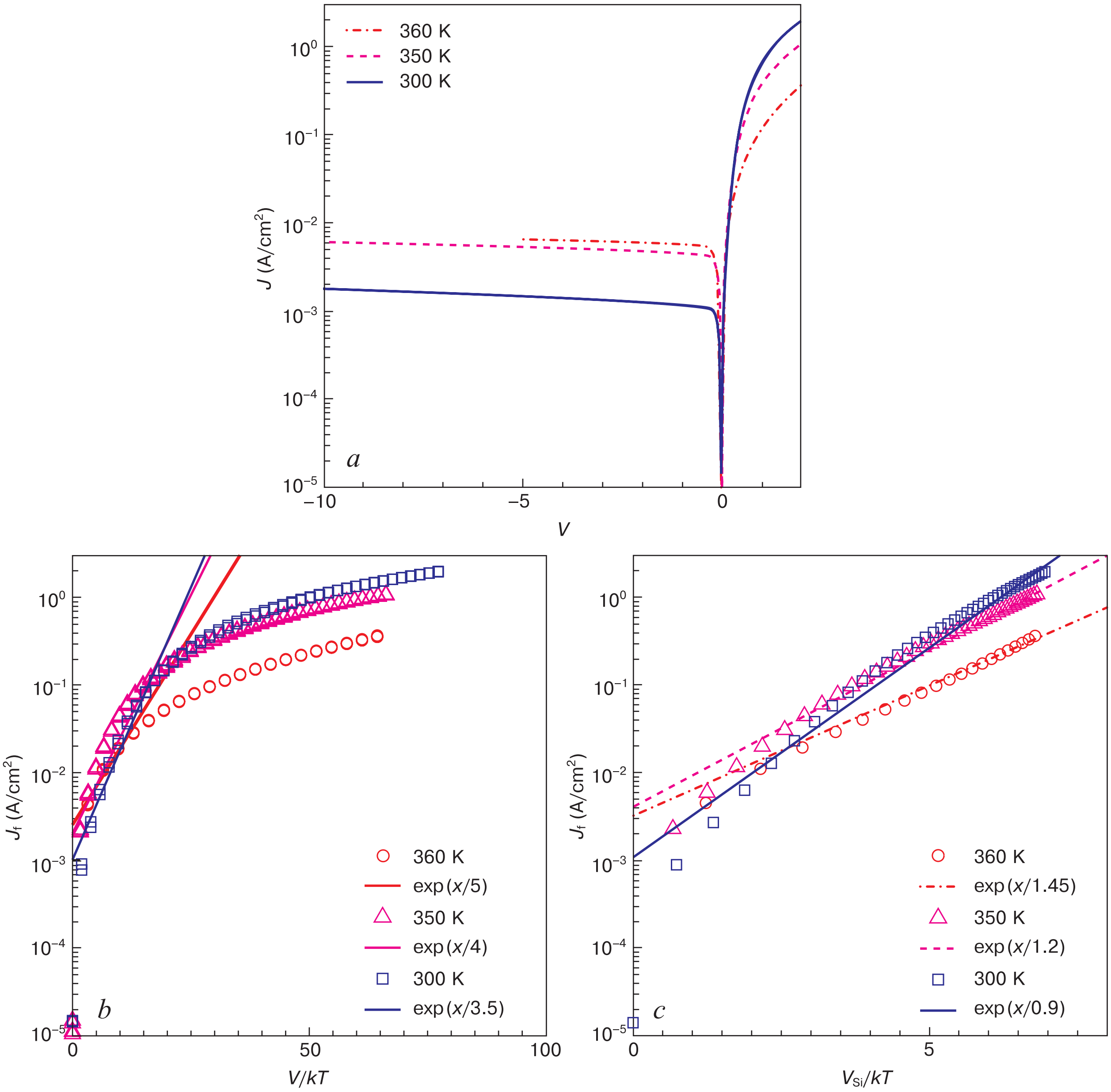

Figure 2. Analysis of Si/In_2O_3 : Er/In-contact structure I–V curves for *n* type conductivity silicon substrates: (*a*) I–V curves for different temperatures for forward (+*V*) and reverse (–*V*) bias; (*b*) approximation of forward (+*V*) currents (J_f) through the barrier as per Eq. (1b); (*c*) corrected approximation of forward (+V_{Si}) currents J_f through the barrier as per Eq. (3)

ergy tail of Boltzmann's electron distribution curve for silicon: the higher the temperature, the more electrons capable of overcoming the barrier and the higher the current, pursuant to the electron thermoemission model [41]. For a sufficiently high forward bias $0.5 < V < 2$ V (Fig. 2 *a*) the band bending in silicon becomes greater than the barrier height (Fig. 3 *a*) and all the carriers, i.e., substrate electrons, can easily overcome the barrier (over-barrier mode). In over-barrier mode the current through the structure is controlled by the resistance of the space charge region **(SCR)** in silicon and the In_2O_3 : Er film resistance. The current *vs* temperature dependence in over-barrier mode is inverse to that for sub-barrier mode, i.e., the current declines with an increase in temperature. This behavior is controlled by the temperature function of the conductivity, more specifically, the carrier mobility: the higher the temperature, the lower the mobility since high-temperature carrier mobility is mainly controlled by carrier scattering at lattice phonons [36].

At a negative (reverse) bias applied to the top In contact, electrons are injected from the metal to the film through the backward barrier (Φ_{eb}) at the In/In_2O_3 : Er interface (Fig. 1 *b*). At sufficiently high temperatures (room and above) the backward currents have a saturated pattern (Fig. 2 *a*) in accordance with the barrier thermoemission model [41]:

$$J = J_s\left[\exp\left(\frac{V}{nkT}\right)-1\right]. \tag{1a}$$

For the forward branch $V > 3kT$ the simplified expression (Eq. (1a)) has an exponential growth pattern:

$$J = J_s \exp\left(\frac{V}{nkT}\right), \tag{1b}$$

where V is the bias, n is the nonideality factor, k is Boltzmann's constant, T is the absolute temperature and J_s is the saturation backward current determined as follows:

$$J_s = A^R T^2 \exp\left(-\frac{\Phi}{kT}\right), \tag{2}$$

where Φ is the barrier height and A^R is Richardson's constant (A^R = 120 A/(cm$^2 \cdot$ K^2) for electrons in silicon and A^R = 30 A/(cm$^2 \cdot$ K^2) for holes in silicon [41]).

Figure 2 *b* shows an exponential approximation of the forward I–V curve branches for low bias (at the sub-barrier section) as per Eq. (1b). It can be seen from Fig. 2 *b* that the initial I–V curve sections can be described with exponents but the nonideality coefficients prove to be excessively large (n = 3÷5). Correct analysis requires taking into account that the n-Si/In_2O_3 : Er/In-contact structure in question is a metal/dielectric/semiconductor **(MDS)** or a metal/oxide/semiconductor **(MOS)** structure where the In_2O_3 : Er is the intermediate dielectric layer between the silicon substrate and the metallic contact. Although In_2O_3 is not a classic dielectric but rather a wide-band semiconductor ($E_{gIn_2O_3}$ = 2.69÷2.93 eV [38, 39]) and has a low electron injection barrier as will be shown below, its barrier current expression (Eq. (1b)) should be corrected.

To correct Eq. (1b) one should take into account that bias applied to an MDS structure drops not only in the silicon SCR but also in the dielectric, with the barrier height decreasing exactly by the magnitude of the silicon potential drop ($\Phi - V_{Si}$), see Fig. 1 *a* and Fig. 3 *a*. Barrier tunneling at lower bias is still low and is therefore ignored. Then the barrier thermoemission expression (Eq. (1b)) for the MDS structure transforms as follows:

$$J = J_s \exp\left(-\frac{V_{Si}}{nkT}\right). \tag{3}$$

The silicon potential drop V_{Si} as a function of the bias V was calculated by numerically solving Poisson's equation in Boltzmann's carrier statistics approximation [41] and is shown in Fig. 3 *b* for different temperatures by solid curves for the KEF 7.5 n type conductivity Si substrate. The respective calculated curves for the Si/SiO_2 system were reported in the cited work [41]. Those curves can be used with a dielectric permeability correction for In_2O_3 ($\varepsilon_{In_2O_3}$ = 8.9 [31, 32]) instead of SiO_2. Reconstructing the I–V curves in the silicon potential drop coordinates (V_{Si}) instead of the applied bias ones (Fig. 2 *c*) provides a good fit between the resultant I–V curves and the exponent described by Eq. (3). The nonideality coefficient is close to unity in this case (Fig. 2 *c*).

Thus the initial (sub-barrier) sections of the forward I–V curves for the n-Si/In_2O_3 : Er structures can be described within the barrier thermoemission model with a silicon potential drop correction of the bias.

3.2. I–V curves of *p*-Si/In_2O_3 : Er structure

Figure 4 *a* shows the I–V curve of structures on p type conductivity silicon substrates (p-Si/In_2O_3 : Er) for room temperature and 280, 300 and 400 K. These curves also demonstrate a rectifying pattern, by analogy with those

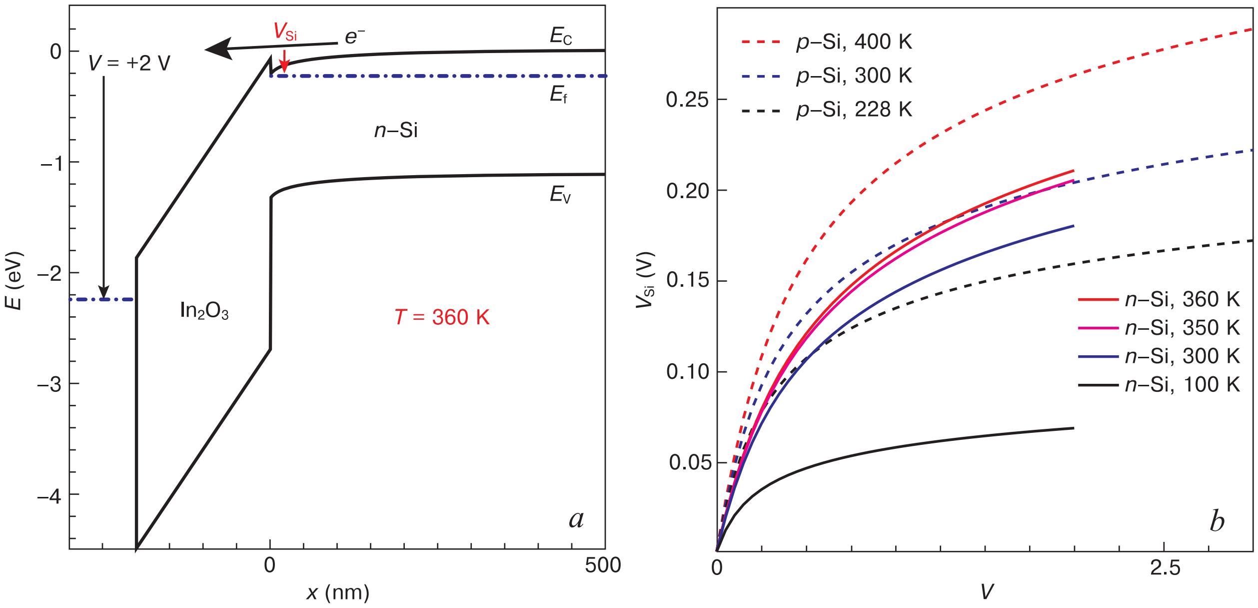

Figure 3. Barrier thermoemission model correction (Eq. (1b)) for silicon potential drop (Eq. (3)): (*a*) band structure calculation in electrostatic approximation (Poisson's equation and Boltzmann's carrier distribution [41]) for T = 360 K; (*b*) $V_{Si}(V)$ calculation for different temperatures T (solid curves are for KEF 7.5 n type conductivity Si substrate and 200 nm In_2O_3 : Er film, dashed curves are for KDB 7.5 p type conductivity Si substrate and 60 nm In_2O_3 : Er film)

for the *n* type conductivity silicon substrate (Fig. 2 *a*) but with an inverse polarity: the forward branch (negative bias) corresponds to hole injection from the *p* type conductivity substrate to the film through the forward barrier Φ_{hf} (Fig. 1 *b*) while the backward branch (positive bias), to hole injection from the surface metal contact to the film through the backward barrier Φ_{hb} (Fig. 1 *a*). The forward I–V curve branch also has a sub-barrier current section from 0 to –1 V and a over-barrier current section from –1 to –3 V (Fig. 4 *a*). By analogy with electron injection, the sub-barrier current for hole injection grows with an increase in temperature following the increase in the concentration of over-barrier energy holes in Boltzmann's distribution. Whereas for electron injection the sub-barrier mode is at 0 to +0.5 V, for hole injection the sub-barrier mode covers a wider range, from 0 to –1 V which may indicate a higher hole injection barrier which is nevertheless lower than it follows from the valence band discontinuity (1.64 eV, see Fig. 1 *b*). The forward over-barrier current in the –1 to –3 V range (Fig. 4 *a*) drops with an increase in temperature by analogy with the case of the *n* type conductivity substrate since it is controlled by the same carrier scattering mechanism, i.e., at lattice phonons [36]. For a reverse bias (0 – +5 V) the currents have a saturating pattern in accordance with the barrier thermoemission model as per Eq. (1a) [41].

By analogy with the electron injection case discussed above (Figs. 2 and 3), hole injection from the *p* type conductivity substrate through the barrier to the $In_2O_3:Er$ film was also analyzed within the barrier thermoemission

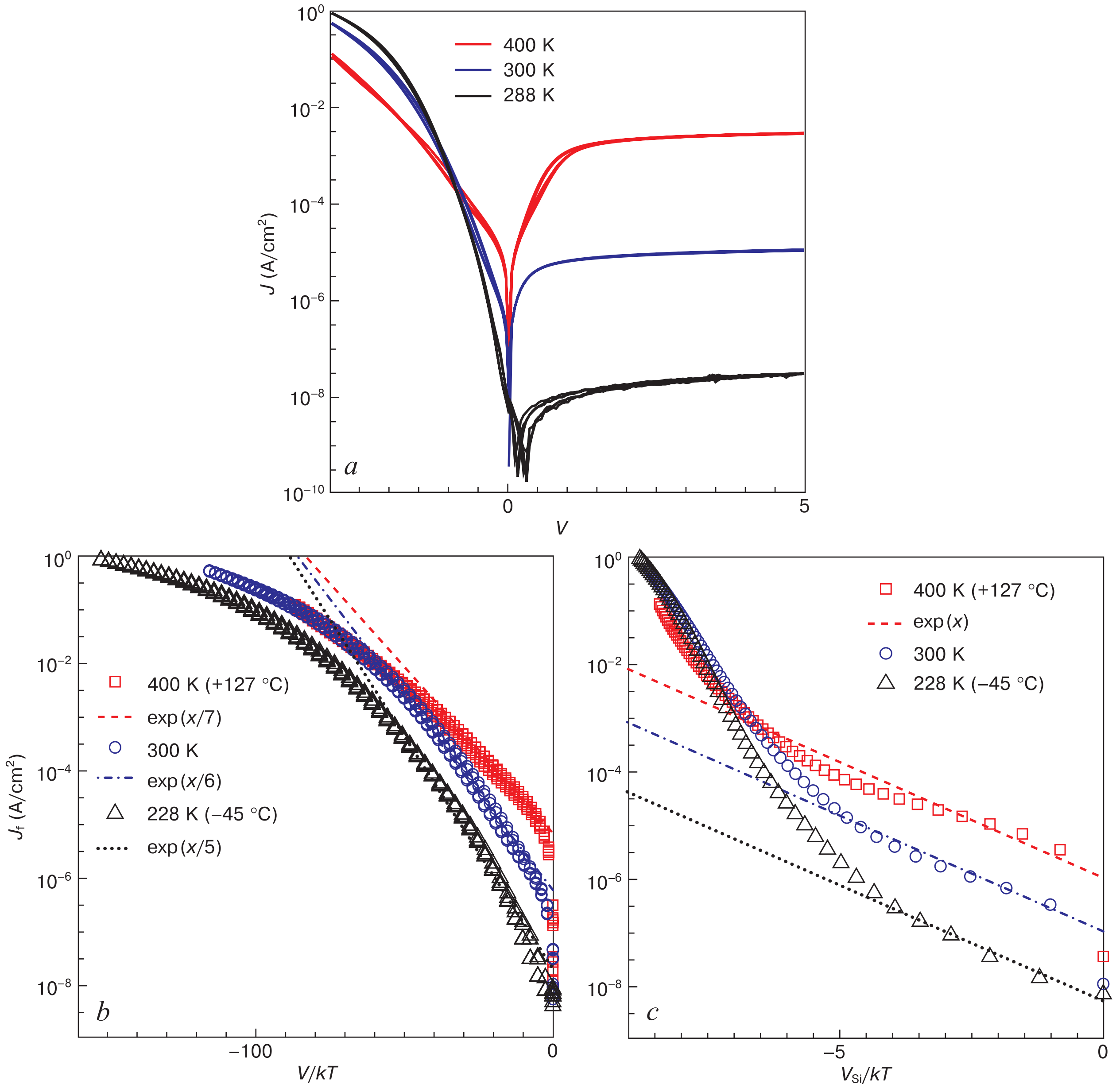

Figure 4. Analysis of $Si/In_2O_3:Er/In$ contact structure I–V curves for *p* type conductivity silicon substrates: (*a*) I–V curves for different temperatures for forward (–*V*) and reverse (+*V*) bias; (*b*) approximation of forward (–*V*) currents (J_f) through the barrier as per Eq. (1b); (*c*) corrected approximation of forward ($-V_{Si}$) currents J_f through the barrier as per Eq. (3)

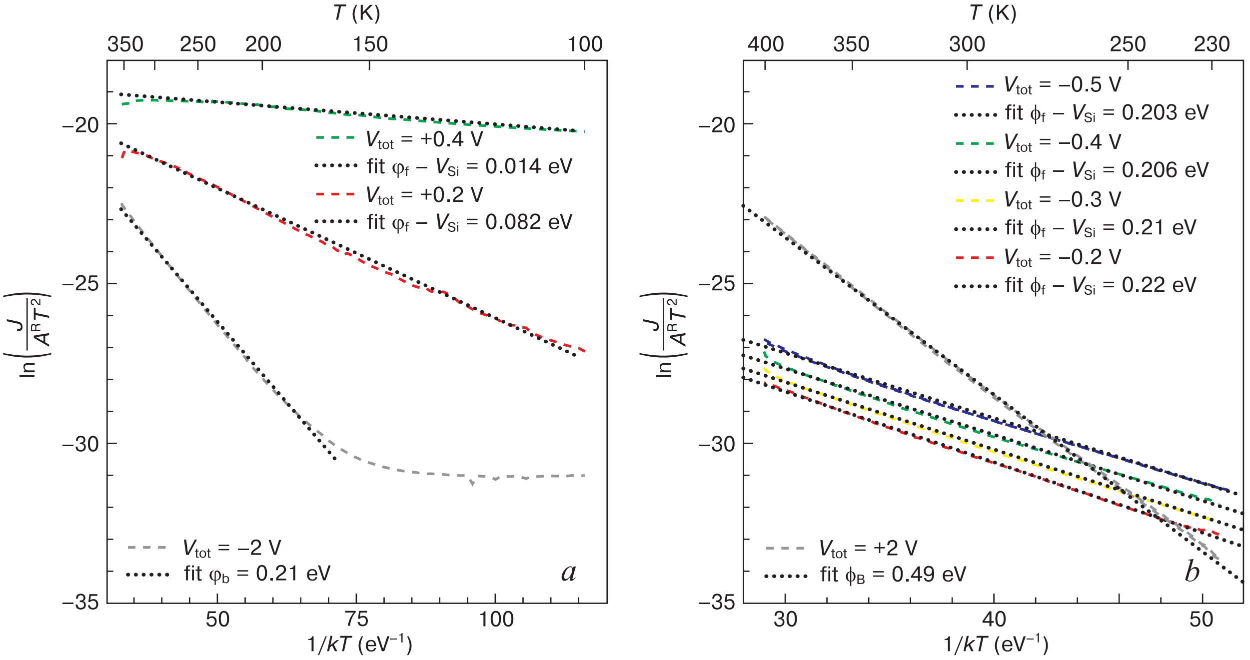

Figure 5. Forward current *vs* temperature functions in Schottky coordinates at low sub-barrier bias (color dashed lines) and backward currents at saturation (gray dashed lines) for $Si/In_2O_3:Er$ strucrures on (*a*) n and (*b*) *p* type conductivity silicon substrates. Slope and barrier height analysis for electron and hole injection

model. Figure 4 *b* shows I–V curve exponential approximation in accordance with uncorrected Eq. (1b). The nonideality coefficients prove to be large (n = 5÷7). Then, by analogy with the solution of Poisson's equation in Boltzmann's carrier statistics approximation, the KDB 7.5 *p* type conductivity Si substrate / 60 nm thick In_2O_3 dielectric MOS structure ($\varepsilon_{In2O3} = 8.9$ [31, 32]) was simulated for different bias ($V = 0 \div -3$ V) and 228, 300 and 400 K. For each bias the silicon potential drop V_{Si} was found. The calculated V_{Si} *vs* V curves are shown in Fig. 3 *b* by dashes. Figure 4 *c* shows the I–V curves for forward currents J_f as a function of silicon potential drop. Then the initial (sub-barrier) sections of the I–V curves can be approximated with exponents in accordance with corrected Eq. (3) and the nonideality coefficients will be close to unity ($n = 1$).

Thus the initial I–V curve sections for the $Si/In_2O_3:Er$ structures on silicon substrates, whether *n* or *p* type conductivity, can be described within the majority carrier barrier thermoemission model with a silicon potential drop correction of the bias.

3.3. Determination of electron injection barrier height between *n* type conductivity silicon substrate and $In_2O_3:Er$ film

To determine the forward electron injection barrier Φ_{ef} between *n* type conductivity silicon and the $In_2O_3:Er$ film (Fig. 1 *a*), we measured the forward current *vs* temperature functions at low bias in sub-barrier mode $V = +0.2$ and +0.4 V (Fig. 2 *a*). To determine the backward electron injection barrier Φ_{eb} between the metallic In contact and the $In_2O_3:Er$ film (Fig. 1 *b*), we measured the backward current *vs* temperature functions at saturation $V = -2$ V (Fig. 2 *a*). The resultant temperature functions were plotted in Schottky coordinates in accordance with Eqs. (2) and (3) (Fig. 5 *a*).

For reverse bias at saturation $V = -2$ V (Fig. 2 *a*), the backward current *vs* temperature function in Schottky coordinates (Fig. 5 *a*, grey dashes) fits a line the slope of which corresponds to the backward electron injection barrier height between the metallic In contact and the $In_2O_3:Er$ film: $\Phi_{eb} = 0.21$ eV (Fig. 1 *b*). At low temperatures ($T < 150$ K, see Fig. 5 *a*) the backward current no longer depends on temperature, probably due to a change of the current mechanism from thermoemision to barrier tunneling.

For low forward sub-barrier bias $V = +0.2$ and +0.4 V (Fig. 2 *a*) the current *vs* temperature functions in Schottky coordinates have 82 and 14 meV slopes, respectively (Fig. 5 *a*, red and green dashed lines) corresponding to the forward barrier height less the silicon potential drop, i.e., $\Phi_{ef} - V_{Si}$ (Fig. 1 *a*). Addition of $V_{Si} = 61$ and 94 mV (Fig. 3 *b*, blue solid line) yields the forward electron injection barrier height between silicon and the films ($n\text{-}Si/In_2O_3:Er$) $\Phi_{ef} = 0.143$ and 0.108 eV, respectively. However, since $V = +0.4$ is already close to the over-barrier mode (Fig. 3 *a*), barrier thermoemission is coupled with barrier tunneling and the thermoemission barrier height $\Phi_{ef} = 0.108$ eV appears to be underestimated. Thus, a more correct barrier height estimate can be obtained in purely sub-barrier mode at low bias $V = +0.2$ V. Thus, the forward electron injection barrier between the silicon substrate and the film ($n\text{-}Si/In_2O_3:Er$) is $\Phi_{ef} = 0.14$ eV.

3.4. Barrier height determination for hole injection to $In_2O_3:Er$ film from p type conductivity silicon substrate

To determine the forward hole injection barrier between p type conductivity silicon and the $In_2O_3:Er$ film (e.g. Φ_{hf} in Fig. 1 *b*), we measured the forward current *vs* temperature functions at low bias in sub-barrier mode $-0.5\ V \le V < 0$ (Fig. 4 *a*). To calculate the backward hole injection barrier between the metallic In contact and the $In_2O_3:Er$ film (e.g. Φ_{hb} in Fig. 1 *a*), we measured the backward current *vs* temperature functions at saturation for $V = 2$ V (Fig. 4 *a*). The resultant temperature functions were plotted in Schottky coordinates in accordance with Eqs. (2) and (3) (Fig. 5 *b*).

For reverse bias at saturation $V = +2$ V (Fig. 4 *a*), the backward current *vs* temperature function in Schottky coordinates (Fig. 5 *b*, grey dashed line) fits a line with a slope corresponding to the backward hole injection barrier height between the metallic In contact and the $In_2O_3:Er$ film: $\Phi_{hb} = 0.5$ eV (Fig. 6 *b*).

For low forward sub-barrier bias $V = -0.2, -0.3, -0.4$ and -0.5 V (Fig. 4 *a*) the current *vs* temperature functions in Schottky coordinates have slopes of 0.22, 0.21, 0.206 and 0.203 meV, respectively (Fig. 5 *b*, color dashed lines) corresponding to the forward barrier height less the silicon potential drop, i.e., $\Phi_{hf} - V_{Si}$ (Fig. 6 *a*). Correction by the calculated $V_{Si} = 0.08$, 0.1, 0.12 and 0.13 V, respectively (Fig. 3 *b*, blue dashed line) yields the forward hole injection barrier height between silicon and the films in the p-$Si/In_2O_3:Er$ structures: $\Phi_{hf} = 0.3$ eV (Fig. 6 *a*).

Thus, the temperature functions of the backward saturation currents and the forward sub-barrier currents for the $In_2O_3:Er$ film structures on n and p type conductivity silicon substrates ($Si/In_2O_3:Er$) suggest that the forward electron injection barrier between n type conductivity silicon and the films (n-$Si/In_2O_3:Er$) is $\Phi_{ef} = 0.14$ eV, the backward electron injection barrier between the metallic In contact and the film ($In/In_2O_3:Er$) is $\Phi_{eb} = 0.21$ eV, the forward hole injection barrier between p type conductivity silicon and the films (p-$Si/In_2O_3:Er$) is $\Phi_{hf} = 0.3$ eV and the backward hole injection barrier between the metallic In contact and the films ($In/In_2O_3:Er$) is $\Phi_{hb} = 0.5$ eV.

3.5. Analysis of $Si/In_2O_3:Er$ heterojunction band structure

The data on carrier injection barriers are shown in the schematic band diagrams of the $Si/In_2O_3:Er$ heterostructure in Fig. 6 for p type conductivity silicon substrate. The conduction band discontinuity between silicon E_C and the film $E_{C_{In_2O_3Er}} - E_{C_{Si}}$ is shown in Fig. 6 to be equal to the calculated electron injection barrier $\Phi_{ef} = 0.14$ eV. This assumption was made on the basis of indirect literary data on low electron injection barriers both for Si/In_2O_3 (e.g., there are data on a negative barrier [33, 34]) and for related materials $Si/In_2O_3:Mo$ [35] and $Si/In_2O_3:Sn$ [31,32]. Judging from the calculated electron injection barrier $\Phi_{ef} = 0.14$ eV, the literary data on the silicon band gap $E_{gSi} = 1.12$ eV [41] and the film band gap $E_{gIn_2O_3} = 2.69 \div 2.93$ eV [38, 39] (we accept it to be 2.9 eV for clarity), the valence band discontinuity between silicon E_V and indium oxide $E_{V_{In_2O_3Er}} - E_{V_{Si}}$ appears to be excessively large, i.e., 1.64 eV (Fig. 1 *b*).

Despite the large calculated valence band discontinuity ($\Delta E_V \sim 1.64$ eV), the hole injection barrier between silicon and the film proved to be but moderate: $\Phi_{hf} = 0.3$ eV (Fig. 6 *a*). This indicates that the band gap of the synthesized films has a hole conduction channel. It is shown by the dotted line E_{ds} in Fig. 6.

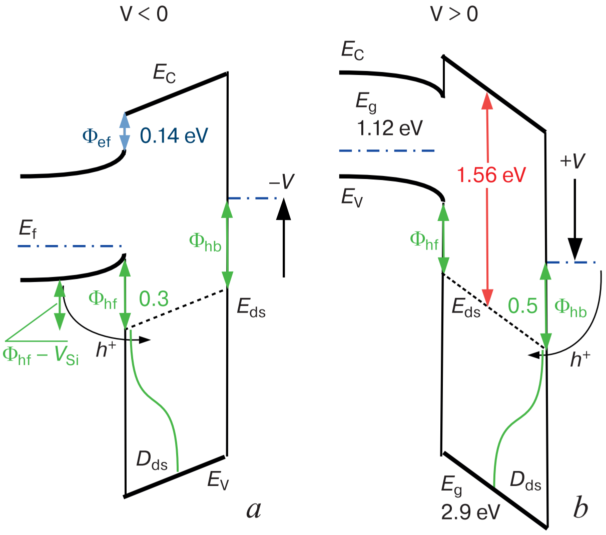

Figure 6. Schematic band diagrams of p-$Si/In_2O_3:Er$ heterostructure for (*a*) forward and (*b*) reverse bias with electron and hole injection barriers shown

It seems that the hole conduction channel in the band gap is associated with the defect states caused by an imperfect structure of the RF magnetron sputtered $In_2O_3:Er$ films. Possibly, high defect concentrations introduced by magnetron deposition form multiple defect levels in the band gap. These multiple defect levels merge to form a defect state density spreading from the valence band edge E_V to the hole conduction channel in the band gap E_{ds}. In Fig. 6 the defect state density in the band gap of the $In_2O_3:Er$ films is schematically shown by the green curve D_{ds}.

Thus, electron transport in the film occurs via the conduction band E_C (Fig. 1 *a*) and hole transport occurs inside the band gap via the conduction channel E_{ds} (Fig. 6 *a*) generated by the tails of the defect state density D_{ds} in the band gap. Taking into account the literary data on the silicon band gap ($E_{gSi} = 1.12$ eV [41]) and the calculated electron and hole injection barriers between silicon and the $In_2O_3:Er$ film, i.e., $\Phi_{ef} = 0.14$ eV and $\Phi_{hf} = 0.3$ eV, respectively (Fig. 6 *a*), the energy gap between the conduction band electrons and the band gap conduction channel holes is $E_C - E_{ds} = 1.56$ eV (Fig. 6 *b*).

3.6. Defect state density in In_2O_3 : Er band gap

The 400–800 nm PL spectra (Fig. 7) confirm the existence of defect levels in the In_2O_3 band gap [42–48]. These levels fall in the 1.55–3.1 eV energy range, i.e., inside the In_2O_3 band gap $E_{\mathrm{gIn_2O_3}} = 2.69 \div 2.93$ eV [38, 39].

In_2O_3 films synthesized using different methods were studied earlier [42–48]:

– metallic In sputtering followed by thermal oxidation [42];

– growth and oxidation in an argon + oxygen gas atmosphere on an InP substrate with gold as surfactant by vapor–liquid–crystal mechanism **(VLS)** [43];

– oxidation of 1–3 mm metallic In grains in an argon + oxygen gas atmosphere [44];

– In evaporation and transport in an argon + oxygen gas atmosphere and deposition on substrate [45];

– In evaporation and redeposition in an argon flow atmosphere in a furnace [46];

– In_2O_3 vapor phase deposition in an argon + oxygen gas atmosphere on a silicon substrate with gold surfactant [47];

– metallic indium deposition on differently oriented silicon substrates ((100), (110), (111)) and 850 °C oxidation in a wet argon flow atmosphere [48].

These methods produce completely different film structures: 400–600 nm nanocrystals consisting of agglomerated finer 40–60 nm nanocrystals [42]; square cross-section 15–150 nm thick nanowires reaching decades of microns in length [43]; 40–120 nm diam. nanowires 15–25 µm in length [44]; 20–100 nm diam. nanowires (30 nm on average) up to 100 µm in length [45]; octahedral faced crystals several microns in size [46]; 20–40 nm diam. nanowires 1 µm in length with gold drops at ends [47]; 0.1–1.0 µm sized polycrystals [48].

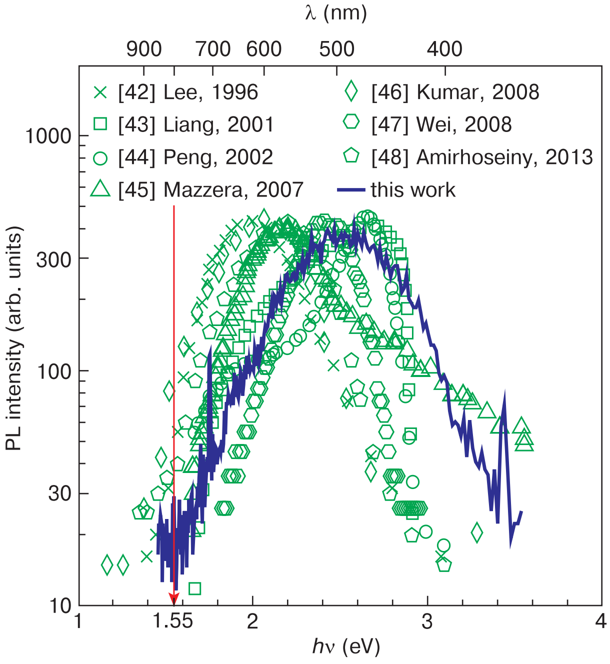

Figure 7. In_2O_3 : Er PL spectra compared against literary data on PL of In_2O_3 films synthesized using different methods [42–48]

The 400–800 nm PL falling into the In_2O_3 band gap was attributed to the following defects in the band gap [42–48]: oxygen deficiency related defects [42]; oxygen vacancies [43]; single-ionized oxygen vacancies $[V_O^+]$ [44]. One of the peaks at 420 nm was attributed [45] to oxygen deficiency related defects $[V_O]$, and the other 630 nm one, to excess oxygen atom related defects, e.g. interstitial oxygen atoms $[O_I]$, In vacancies $[V_{In}]$ or In atoms substituted for O $[O_{In}]$ [45]. In another work [46] PL was attributed to interstitial In atoms $[In_i^{3+}]$ rather than oxygen vacancies, while in [47, 48], again to oxygen vacancies. Thus the defect origin is most often reported to be oxygen atom deficiency, but exceptions occur [45]. However, the specific defect type is most often reported to be oxygen vacancy, the authors not having a general consensus though.

Similar 400–800 nm PL is observed in our magnetron sputtered films (Fig. 7, blue curve). The PL absorption edge 1.55 eV (Fig. 7) is in a good agreement with the energy gap between the electrons and the holes $E_C - E_{ds}$ = 1.56 eV (Fig. 6 *b*). The electrons are in the conduction band E_C In_2O_3 : Er, and the holes are in the conduction channel E_{ds} caused by the defect state density D_{ds} spreading from the valence band edge E_V to inside the In_2O_3 : Er band gap (Fig. 6 *b*). Thus, the defect state density D_{ds} (Fig. 6) in the band gap is confirmed by PL and accounts for the low hole injection barrier obtained for our structures.

4. Conclusion

In_2O_3 : Er films were RF magnetron sputtered on silicon substrates.

The I–V curves for the structures (Si/In_2O_3 : Er) on *n* and *p* type conductivity silicon substrates have rectifying patterns and at low bias can be described within the majority carrier barrier thermoemission model with a silicon potential drop V_{Si} correction of the bias V.

The electron injection barrier between *n* type conductivity silicon and films (*n*-Si/In_2O_3 : Er) was found to be $\Phi_{ef} = 0.14$ eV and the hole injection barrier between *p* type conductivity silicon and films (*p*-Si/ In_2O_3 : Er), $\Phi_{hf} = 0.3$ eV.

The band structure of the Si/ In_2O_3 : Er heterojunction has a small conduction band discontinuity, $\Delta E_C = 0.14$ eV and a large valence band discontinuity, $\Delta E_V = 1.64$ eV. However, the presence of the hole conduction channel E_{ds} in the In_2O_3 : Er band gap caused by the defect state density tail D_{ds}, spreading from the valence band to the band gap provides for a low hole injection barrier, $\Phi_{hf} = E_{ds} - E_{VSi} = 0.3$ eV. The energy gap between the conduction band electrons and the band gap conduction channel holes is $E_C - E_{ds} = 1.56$ eV.

The presence of the defect state density D_{ds} in the $In_2O_3:Er$ band gap is confirmed by the PL data for the respective 1.55–3.0 eV energy range.

Acknowledgements

Optical measurements were conducted under State Assignment FWGW-2022-00005. The work was financially supported by the FSI (Grant 4235GS1/70543 as of 27.10.2021) and by the Ministry of Science and Higher Education of the Russian Federation (Project No. 075-15-2020-797 (13.1902.21.0024)). Electrical measurements were carried out on facilities of the VTAN Joint Use Center of the Novosibirsk State University. Part of optical measurements were conducted on equipment of the Joint Use Center for High-Resolution Spectroscopy of Gases and Condensed Media of the Institute of Automation and Electrometry, Siberian Branch of the Russian Academy of Sciences. Films were deposited at the Siberian Center for Synchrotron and Terahertz Radiation Joint Use Center on the VEPP-4–VEPP-2000 Complex Unique Research Installation of the Institute of Nuclear Physics, Siberian Branch of the Russian Academy of Sciences. The sputtering target was manufactured by Phildal Holding Co., Ltd., China.

The Authors are grateful to E.D. Zhanaev and N.V. Dudchenko for chemical and thermal treatment of the specimens.

References

1. Sun C., Wade M., Lee Y., Orcutt J.S., Alloatti L., Georgas M.S., Waterman A.S., Shainline J.M., Avizienis R.R., Lin S., Moss B.R., Kumar R., Pavanello F., Atabaki A.H., Cook H.M., Ou A.J., Leu J.C., Chen Y.-H., Asanović K., Ram R.J., Popović M.A., Stojanović V.M. Single-chip microprocessor that communicates directly using light. *Nature*. 2015; 528: 534–538. https://doi.org/10.1038/nature16454
2. Atabaki A.H., Moazeni S., Pavanello F., Gevorgyan H., Notaros J., Alloatti L., Wade M.T., Sun Ch., Kruger S.A., Al Qubaisi H.M.K., Wang I., Zhang B., Khilo A., Baiocco Ch.V., Popović M.A., Stojanović V.M., Rajeev J. Ram Integrating photonics with silicon nanoelectronics for the next generation of systems on a chip. *Nature*. 2018; 556, 349–354. https://doi.org/10.1038/s41586-018-0028-z
3. Cornet Ch., Léger Y., Robert C. Integrated lasers on silicon. Elsevier Ltd.; 2016. 178 p. https://doi.org/10.1016/C2015-0-01237-0
4. Di L., Kurczveil G., Huang X., Zhang C., Srinivasan S., Huang Z., Seyedi M.A., Norris K., Fiorentino M., Bowers J.E., Beausoleil R.G. Heterogeneous silicon light sources for datacom applications. *Optical Fiber Technology*. 2018; 44: 43–52. https://doi.org/10.1016/j.yofte.2017.12.005
5. Norman J.C., Jung D., Wan Y., Bowers J.E. Perspective: The future of quantum dot photonic integrated circuits. *APL Photonics*. 2018; 3: 030901. https://doi.org/10.1063/1.5021345
6. Jung D., Norman J., Wan Y., Liu S., Herrick R., Selvidge J., Mukherjee K., Gossard A.C., Bowers J.E. Recent advances in InAs quantum dot lasers grown on on-axis (001) silicon by molecular beam epitaxy. *Physica Status Solidi (A)*. 2019; 216(1): 1800602. https://doi.org/10.1002/pssa.201800602
7. Jung D., Herrick R., Norman J., Turnlund K., Jan C., Feng K., Gossard A.C., Bowers J.E. Impact of threading dislocation density on the lifetime of InAs quantum dot lasers on Si. *Applied Physics Letters*. 2018; 112(15): 153507. https://doi.org/10.1063/1.5026147
8. Mukherjee K., Selvidge J., Jung D., Norman J., Taylor A.A., Salmon M., Liu A.Y., Bowers J.E., Herrick R.W. Recombination-enhanced dislocation climb in InAs quantum dot lasers on silicon. *Journal of Applied Physics*. 2020; 128(2): 025703. https://doi.org/10.1063/1.5143606
9. Shang C., Hughes E., Wan Y., Dumont M., Koscica R., Selvidge J., Herrick R., Gossard A.C., Mukherjee K., Bowers J.E. High-temperature reliable quantum-dot lasers on Si with misfit and threading dislocation filters. *Optica*. 2021; 8(5): 749–754. https://doi.org/10.1364/OPTICA.423360
10. Carnall W.T., Fields P.R., Rajnak K. Electronic energy levels in the trivalent lanthanide aquo ions. I. Pr^{3+}, Nd^{3+}, Pm^{3+}, Sm^{3+}, Dy^{3+}, Ho^{3+}, Er^{3+}, and Tm^{3+}. *The Journal of Chemical Physics*. 1968; 49(10): 4424–4442. http://dx.doi.org/10.1063/1.1669893
11. Gruber J.B., Henderson J.R., Muramoto M., Rajnak K., Conway J.G. Energy levels of single-crystal erbium oxide. *The Journal of Chemical Physics*. 1966; 45(2): 477–482. http://dx.doi.org/10.1063/1.1727592
12. Ennen H., Schneider J., Pomrenke G., Axmann A. 1.54 mkm luminescence of erbium implanted III–V semiconductors and silicon. *Applied Physics Letters*. 1983; 43(10): 943–945. http://dx.doi.org/10.1063/1.94190
13. Polman A. Erbium implanted thin film photonic materials. *Journal of Applied Physics*. 1997; 82(1): 1–39. https://doi.org/10.1063/1.366265
14. Kenyon A.J. Topical review: Erbium in silicon. *Semiconductor Science and Technology*. 2005; 20(12): R65–R84. https://doi.org/10.1088/0268-1242/20/12/R02
15. Coffa S., Franz`o G., Priolo F. Mechanism and performance of forward and reverse bias electroluminescence at 1.54 μm from Er-doped Si diodes. *Journal of Applied Physics*. 1997; 81(6): 2784–2793. https://doi.org/10.1063/1.363935
16. Coffa S., Franzò G., Priolo F. High efficiency and fast modulation of Er-doped light emitting Si diodes. *Applied Physics Letters*. 1996; 69(14): 2077–2079. https://doi.org/10.1063/1.116885
17. Polman A., van den Hoven G.N., Custer J.S., Shin J.H., Serna R., Alkemade P.F.A. Erbium in crystal silicon: Optical activation, exci-

tation, and concentration limits. *Journal of Applied Physics*. 1995; 77(3): 1256–1262. https://doi.org/10.1063/1.358927

18. Gusev O.B., Bresler M.S., Pak P.E., Yassievich I.N., Forcales M., Vinh N.Q., Gregorkiewicz T. Excitation cross section of erbium in semiconductor matrices under optical pumping. *Physical Review B*. 2001; 64(7): 075302. https://doi.org/10.1103/PhysRevB.64.075302
19. Priolo F., Franzo G., Coffa S., Carnera A. Excitation and nonradiative deexcitation processes of Er^{3+} in crystalline Si. *Physical Review B*. 1998; 57(8): 4443. https://doi.org/10.1103/PhysRevB.57.4443
20. Coffa S., Franz G., Priolo F., Polman A., Serna R. Temperature dependence and quenching processes of the intra-4f luminescence of Er in crystalline Si. *Physical Review B*. 1994; 49(23): 16313. https://doi.org/10.1103/PhysRevB.49.16313
21. Bradley J.D.B., Pollnau M. Erbium-doped integrated waveguide amplifiers and lasers. *Laser & Photonics Reviews*. 2011; 5(3): 368–403. https://doi.org/10.1002/lpor.201000015
22. Wang S., Eckau A., Neufeld E., Carius R., Buchal Ch. Hot electron impact excitation cross-section of Er^{3+} and electroluminescence from erbium-implanted silicon metal-oxide-semiconductor tunnel diodes. *Applied Physics Letters*. 1997; 71(19): 2824–2826. https://doi.org/10.1063/1.120147
23. Krzyzanowska H., Ni K.S., Fu Y., Fauchet P.M. Electroluminescence from Er-doped SiO_2/nc-Si multilayers under lateral carrier injection. *Materials Science and Engineering: B*. 2012; 177(17): 1547–1550. https://doi.org/10.1016/j.mseb.2011.12.032
24. Berencen Y., Illera S., Rebohle L., Ramirez J.M., Wutzler R., Cirera A., Hiller D., Rodríguez J.A., Skorupa W., Garrido B. Luminescence mechanism for Er^{3+} ions in a silicon-rich nitride host under electrical pumping. *Journal of Physics D: Applied Physics*. 2016; 49(8): 085106. https://doi.org/10.1088/0022-3727/49/8/085106
25. Zhu C., Lv C., Gao Z., Wang C., Li D., Ma X., Yang D. Multicolor and near-infrared electroluminescence from the light-emitting devices with rare-earth doped TiO_2 films. *Applied Physics Letters*. 2015; 107(13): 131103. https://doi.org/10.1063/1.4932064
26. Yang Y., Li Y., Xiang L., Ma X., Yang D. Low-voltage driven ~1.54 µm electroluminescence from erbium-doped ZnO/p^+-Si heterostructured devices: Energy transfer from ZnO host to erbium ions. *Applied Physics Letters*. 2013; 102(18): 181111. http://dx.doi.org/10.1063/1.4804626
27. Yang Y., Jin L., Ma X., Yang D. Low-voltage driven visible and infrared electroluminescence from light-emitting device based on Er-doped TiO_2/p^+-Si heterostructure. *Applied Physics Letters*. 2012; 100(3): 031103. http://dx.doi.org/10.1063/1.3678026
28. Kim H.K., Li C.C., Nykolak G., Becker P.C. Photoluminescence and electrical properties of erbium-doped indium oxide films prepared by RF sputtering. *Journal of Applied Physics*. 1994; 76(12): 8209–8211. https://doi.org/10.1063/1.357882
29. Xiao Q., Zhu H., Tu D., Ma E., Chen X. Near-infrared-to-near-infrared downshifting and near-infrared-to-visible upconverting luminescence of Er^{3+}-doped In_2O_3 nanocrystals. *The Journal of Physical Chemistry C*. 2013; 117(20): 10834–10841. http://dx.doi.org/10.1021/jp4030552
30. Feklistov K.V., Lemzyakov A.G., Prosvirin I.P., Gismatulin A.A., Shklyaev A.A., Zhivodkov Y.A., Krivyakin G.K., Komonov A.I., Kozhukhov A.S., Spesivsev E.V., Gulyaev D.V., Abramkin D.S., Pugachev A.M., Esaev D.G., Sidorov G.Yu. Nanowired structure, optical properties and conduction band offset of RF magnetron-deposited n-Si/In_2O_3 : Er films. *Materials Research Express*. 2020; 7(12): 25903. https://doi.org/10.1088/2053-1591/abd06b
31. Tahar R.B.H., Ban T., Ohya Y., Takahashi Y. Tin doped indium oxide thin films: Electrical properties. *Journal of Applied Physics*. 1998; 83(5): 2631–2645. https://doi.org/10.1063/1.367025
32. Hamberg I., Granqvist C.G. Evaporated Sn-doped In_2O_3 films: Basic optical properties and applications to energy-efficient windows. *Journal of Applied Physics*. 1986; 60(11): R123–R159. https://doi.org/10.1063/1.337534
33. Hoffling B., Schleife A., Fuchs F., Rödl C., Bechstedt F. Band lineup between silicon and transparent conducting oxides. *Applied Physics Letters*. 2010; 97(3): 032116. https://doi.org/10.1063/1.3464562
34. Wang E.Y., Hsu L. Determination of electron affinity of In_2O_3 from its heterojunction photovoltaic properties. *Journal of the Electrochemical Society*. 1978; 125: 1328–1331. https://doi.org/10.1149/1.2131672
35. Zhang X., Zhang Q., Lu F. Energy band alignment of an In_2O_3 : Mo/Si heterostructure. *Semiconductor Science and Technology*. 2007; 22(8): 900–904. https://doi.org/10.1088/0268-1242/22/8/013
36. Weiher R.L. Electrical properties of single crystals of indium oxide. *Journal of Applied Physics*. 1962; 33(9): 2834–2839. https://doi.org/10.1063/1.1702560
37. Zhang D.H., Li C., Han S., Liu X.L., Tang T., Jin W., Zhou C.W. Electronic transport studies of single-crystalline In_2O_3 nanowires. *Applied Physics Letters*. 2003; 82(1): 112–114. https://doi.org/10.1063/1.1534938
38. Weiher R.L., Ley R.P. Optical properties of indium oxide. *Journal of Applied Physics*. 1966; 37(1): 299–302. http://dx.doi.org/10.1063/1.1707830
39. King P.D.C., Veal T.D., Fuchs F., Wang Ch.Y., Payne D.J., Bourlange A., Zhang H., Bell G.R., Cimalla V., Ambacher O., Egdell R.G., Bechstedt F., McConville C.F. Band gap, electronic structure, and surface electron accumulation of cubic and rhombohedral In_2O_3. *Physical Review B*. 2009; 79(20): 205211. https://doi.org/10.1103/PhysRevB.79.205211
40. Kern W., Puotinen D.A. Cleaning solutions based on hydrogen peroxide for use in silicon semiconductor technology. *RCA Review*. 1970; 31: 187–206. https://www.americanradiohistory.com/ARCHIVE-RCA/RCA-Review/RCA-Review-1970-Jun.pdf
41. Sze C.M. Physics of semiconductor devices. In 2 books. John Willey and Sons; 1981. Book 1. 456 p. (Russ. Transl. Zi S. Fizika poluprovodnikovykh priborov. V 2 kn. Moscow: Mir; 1984. Kn. 1. 456 p.)
42. Lee M.S., Choi W.C., Kim E.K., Kim C.K., Min S.K. Characterization of the oxidized indium thin films with thermal oxidation. *Thin Solid Films*. 1996; 279(1-2): 1–3. https://doi.org/10.1016/0040-6090(96)08742-1

43. Liang C., Meng G., Lei Y., Phillipp F., Zhang L. Catalytic growth of semiconducting In_2O_3 nanofibers. *Advanced Materials*. 2001; 13(17): 1330–1333. https://doi.org/10.1002/1521-4095(200109)13:17<1330::AID-ADMA1330>3.0.CO;2-6

44. Peng X., Meng G., Zhang J., Wang X., Wang Y., Wang C., Zhang L. Synthesis and photoluminescence of single-crystalline In_2O_3 nanowires. *Journal of Materials Chemistry*. 2002; (12): 1602–1605. https://doi.org/10.1039/B111315A

45. Mazzera M., Zha M., Calestani D., Zappettini A., Salviati G., Zanotti L. Low-temperature In_2O_3 nanowire luminescence properties as a function of oxidizing thermal treatments. *Nanotechnology*. 2007; 18(35): 355707. http://dx.doi.org/10.1088/0957-4484/18/35/355707

46. Kumar M., Singh V.N., Singh F., Lakshmi K.V., Mehta B.R., Singh J.P. On the origin of photoluminescence in indium oxide octahedron structures. *Applied Physics Letters*. 2008; 92(17): 171907. https://doi.org/10.1063/1.2910501

47. Wei Z.P., Guo D.L., Liu B., Chen R., Wong L.M., Yang W.F., Wang S.J., Sun H.D., Wu T. Ultraviolet light emission and excitonic fine structures in ultrathin single-crystalline indium oxide nanowires. *Applied Physics Letters*. 2010; 96(3): 031902. https://doi.org/10.1063/1.3284654

48. Amirhoseiny M., Hassan Z., Shashiong N. Synthesis of nanocrystalline In_2O_3 on different Si substrates at wet oxidation environment. *Optik*. 2013; 124(17): 2679–2681. https://doi.org/10.1016/j.ijleo.2012.08.073